

Structural and optical properties of three-dimensional $\text{Si}_{1-x}\text{Ge}_x/\text{Si}$ nanostructures

D J Lockwood¹, J-M Baribeau¹, B V Kamenev², E-K Lee² and L Tsybeskov²

¹ Institute for Microstructural Sciences, National Research Council Canada, Ottawa, ON K1A 0R6, Canada

² Department of Electrical and Computer Engineering, New Jersey Institute of Technology, University Heights, Newark, NJ 07102, USA

E-mail: david.lockwood@nrc-cnrc.gc.ca

Received 5 July 2007, in final form 13 August 2007

Published 12 May 2008

Online at stacks.iop.org/SST/23/064003

Abstract

Steady-state and time-resolved photoluminescence (PL) combined with x-ray and Raman measurements have been performed on a series of well-characterized $\text{Si}_{1-x}\text{Ge}_x/\text{Si}$ superlattice samples with an island-like morphology and with precise control over the alloy chemical composition in the range $0.091 \leq x \leq 0.61$. In the samples with x increasing from 0.091 to 0.53, an increase in the intensity of the Raman signal related to Ge–Ge vibrations correlates with a red shift in the PL peak position and an increase in the activation energy of the PL thermal quenching. Time-resolved PL measurements reveal two PL components with relaxation times of a microsecond and up to 10 ms, respectively. The highest PL quantum efficiency observed (better than 1% at low temperature) is found in the samples with $x \approx 0.5$ where carrier recombination presumably occurs at sharp $\text{Si}/\text{Si}_{1-x}\text{Ge}_x$ interfaces which exhibit type-II band alignment, with a small (of the order of several milli-electron volts) barrier for electrons and deep potential wells for holes localized within Ge-rich $\text{Si}_{1-x}\text{Ge}_x$ islands. In the samples with Ge concentration close to 0.61, we observe a strong, step-like increase in strain and significant evidence of strain-induced Si/Ge interdiffusion resulting in a decrease of the PL quantum efficiency.

(Some figures in this article are in colour only in the electronic version)

1. Introduction

The indirect band structure of crystalline Si (c-Si) prevents its use in optoelectronic devices and specifically in light emitters [1]. A number of routes have been explored to increase the efficiency of radiative electron–hole recombination in Si-based materials. Among them are quantum confinement in nanometer size Si nanocrystals [2], Si doping by rare-earth [3, 4] and isoelectronic impurities [5, 6], and band structure engineering in $\text{Si}_{1-x}\text{Ge}_x/\text{Si}$ nanostructures [7, 8]. $\text{Si}_{1-x}\text{Ge}_x/\text{Si}$ is one of the most promising material systems for the development of optoelectronic devices in the important optical communication wavelength region of 1.3–1.5 μm , mainly because these structures can easily be incorporated

into the complementary metal oxide semiconductor (CMOS) environment. The problem of a 4.2% lattice mismatch between crystalline Si and Ge can be solved by (i) forming a three-dimensional (3D) island-like surface morphology, which partially relaxes the strain without inducing defect formation [9–12] and (ii) control over the Ge composition x in $\text{Si}_{1-x}\text{Ge}_x$ islands [13–16]. In these structures, efficient photoluminescence (PL) is expected due to the strong selection rule reduction in small-size $\text{Si}_{1-x}\text{Ge}_x$ alloy islands [14, 17, 18]. This paper reports detailed studies by x-ray diffraction and reflection and Raman scattering combined with PL (steady-state and time-resolved) spectroscopy of the optical properties of $\text{Si}_{1-x}\text{Ge}_x$ islands embedded into a Si matrix with x controllably varied from $0.091 \leq x \leq 0.61$.

Table 1. Growth and physical data on the $\text{Si}_{1-x}\text{Ge}_x/\text{Si}$ multilayer samples, where x is the nominal Ge composition, t_{Si} the nominal thickness of the Si spacer layers, t_{SiGe} is the nominal thickness of the $\text{Si}_{1-x}\text{Ge}_x$ layers, N is the number of periods, T_{growth} is the growth temperature, R_{Si} is the Si deposition rate, R_{Ge} is the Ge deposition rate and σ_{Si} and σ_{Ge} are the Si to $\text{Si}_{1-x}\text{Ge}_x$ and $\text{Si}_{1-x}\text{Ge}_x$ to Si interface roughness, respectively, as determined from x-ray reflectance studies.

x	t_{Si} (nm)	t_{SiGe} (nm)	N	T_{growth} (°C)	R_{Si} (nm s ⁻¹)	R_{Ge} (nm s ⁻¹)	σ_{Si} (nm)	σ_{Ge} (nm)
0.091	27	3.8	20	595	0.2	0.05	0.5	0.7
0.17	34	7.0	15	595	0.2	0.05	0.5	0.9
0.53	15	3.5	10	625	0.075	0.09	0.6	0.9
0.56	13.6	3.0	10	640	0.07	0.09	0.7	1.0
0.61	14.1	3.0	10	650	0.07	0.09	—	—

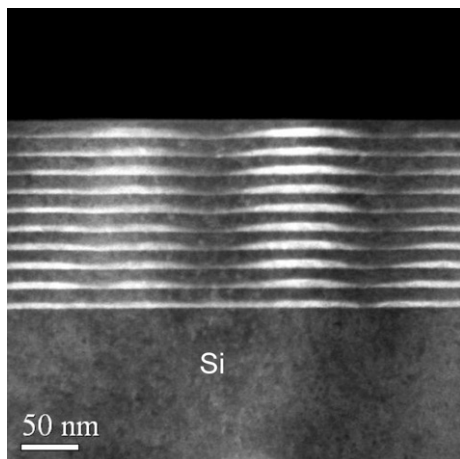


Figure 1. A high-contrast TEM micrograph showing a cross-section of a multilayer $\text{Si}_{1-x}\text{Ge}_x$ island sample with $x = 0.56$. The image is obtained in high-angle annular dark field imaging conditions.

2. Sample growth and structural characterization

The samples used in this study were grown by molecular beam epitaxy (MBE) in a VG Semicon V80 system using a methodology described elsewhere [19, 20]. Details of the samples are given in table 1. The $\text{Si}_{1-x}\text{Ge}_x$ nominal composition x and layer thicknesses in the multilayers with a low Ge content were estimated from an analysis of their x-ray rocking curves. Transmission electron microscopy (TEM) studies (see, e.g., figure 1) have shown that the $\text{Si}_{1-x}\text{Ge}_x/\text{Si}$ multilayers with Ge-rich layers ($x \geq 0.5$) exhibit an island-like morphology (i.e. 3D growth) with vertically aligned $\text{Si}_{1-x}\text{Ge}_x$ undulations [21, 22]. In these growth regimes, x-ray simulations did not yield reliable growth parameters and the thicknesses and compositions of the layers were estimated from atomic fluxes (typically in the range 0.05–0.1 nms⁻¹) and the shutter-time sequencing used during deposition. All the samples discussed here were grown in the temperature range 590–650 °C, as measured by infrared pyrometry to an accuracy of ± 25 °C.

Insight into the structural properties of the various multilayers studied here was obtained by x-ray scattering experiments. These measurements were performed using a Bruker D8 Discover diffraction system equipped with a Goebel mirror on the primary optics and using Cu K α radiation.

High resolution (004) rocking curves were recorded using a four-bounce channel-cut Ge (220) monochromator at a resolution of 12 arcsec. Reciprocal space maps (RSMs) of the (004) reflection were recorded by using a three-bounce channel-cut Ge (220) analyzer at a resolution of 12 arcsec. Grazing incidence specular reflectometry was performed using an asymmetric four-bounce channel-cut Ge (220) monochromator (35 arcsec resolution) as a primary optic and the Ge analyzer as the receiving optic. In all measurements, the scattering plane was parallel to a [110] Si crystallographic direction. Rocking curves were simulated using the dynamical x-ray diffraction theory, while reflectivity profiles were calculated using a multilayer algorithm based on Parrat's formalism [23]. All calculations were performed using the Leptos 4 simulation package.

Figure 2 compares the (004) rocking curves from three $\text{Si}_{1-x}\text{Ge}_x/\text{Si}$ multilayers with $0.09 < x < 0.55$. The diffraction data from the sample with the lower Ge composition are very well reproduced by the calculation using the structural parameters of table 1. The agreement for the sample of intermediate composition is also good, but a damping of the higher order satellites (near $2\theta = 66^\circ$) indicates a loss of coherence of the superperiodicity due either to thickness irregularities or loss of interface sharpness. No good simulation of the data could be obtained for samples with high Ge composition ($x > 0.5$). Here the satellites remain relatively sharp, but they are broadened at the base and the usual thickness fringes between the peaks are not observed. The result shown here is typical of superlattices exhibiting undulated interface morphology such as that depicted in figure 1 [24]. Although the sample shown here has a nominal Ge composition of 0.53, a better fit was obtained using a lower Ge composition; here, in figure 2(c), a value of $x = 0.42$ was used. Although the conventional diffraction theory of layered media cannot accurately model structures with non-planar interfaces, the lower Ge composition found here points to Si–Ge atomic exchange during the island formation. This aspect has been discussed in detail elsewhere [25, 26].

Figure 3 presents the specular reflectivity curves measured on the same samples as in figure 2. As for the rocking curves, reflectivity curves exhibit satellites arising from the periodic nature of the multilayers. Here, however, the contrast is primarily caused by the modulation of the atomic number in the growth direction rather than by the strain, and analysis of the reflectivity provides complementary information on the surface and interface roughness. Also shown in figure 3

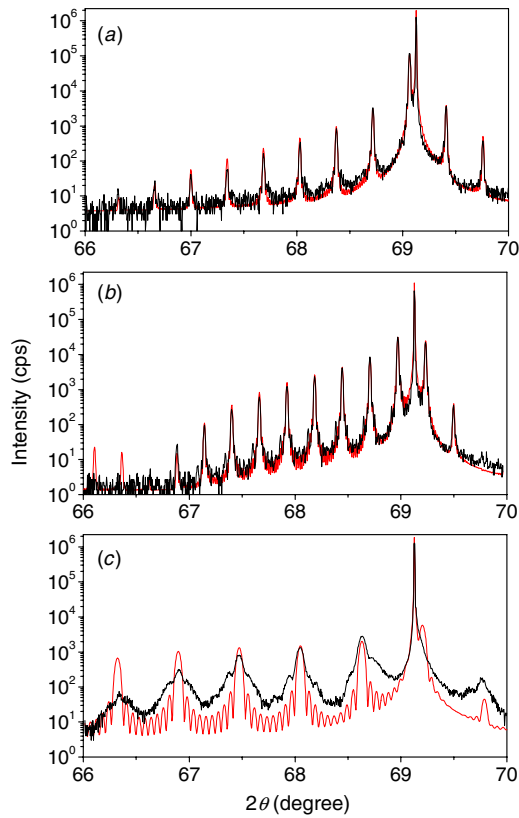


Figure 2. Experimental (black line) and simulated (red/grey line) (004) rocking curves from the $\text{Si}_{1-x}\text{Ge}_x/\text{Si}$ multilayers with (a) $x = 0.09$, (b) $x = 0.17$ and (c) $x = 0.53$. Note that in the latter case, the calculation shown here corresponds to $x = 0.42$.

are simulated profiles obtained with the same values for the thicknesses and compositions used in the rocking curve simulations of figure 2 (see table 1). Here, the interface abruptness is an additional fitting parameter that is taken into account in the calculations by introducing a phenomenological Debye–Waller interface roughness parameter σ at each individual interface [27]. Simulations obtained by assigning constant values for the interface roughnesses σ_{Si} and σ_{Ge} to all Si to $\text{Si}_{1-x}\text{Ge}_x$ and $\text{Si}_{1-x}\text{Ge}_x$ to Si interfaces, respectively, are in qualitative agreement with the experiment. In all cases, a departure between experiment and calculation is seen at higher angles of incidence and is the result of superlattice irregularities and/or interface blurring. Based on the simulations, the value of σ_{Ge} is systematically larger than that of σ_{Si} and the difference increases for higher Ge concentrations, consistent with the evolution of the alloy layers into a 3D morphology in Ge-rich structures.

Additional information on the spatial coherence of the interfaces in multilayers can be obtained by recording the x-ray scattered intensity about a strong diffraction peak in a RSM. Figure 4 compares the (004) RSM from the various samples investigated here. In these maps, the horizontal direction h corresponds to the x-ray wave vector component in a direction parallel to the surface, while the vertical direction ℓ is the wave vector component in the growth direction. While the rocking

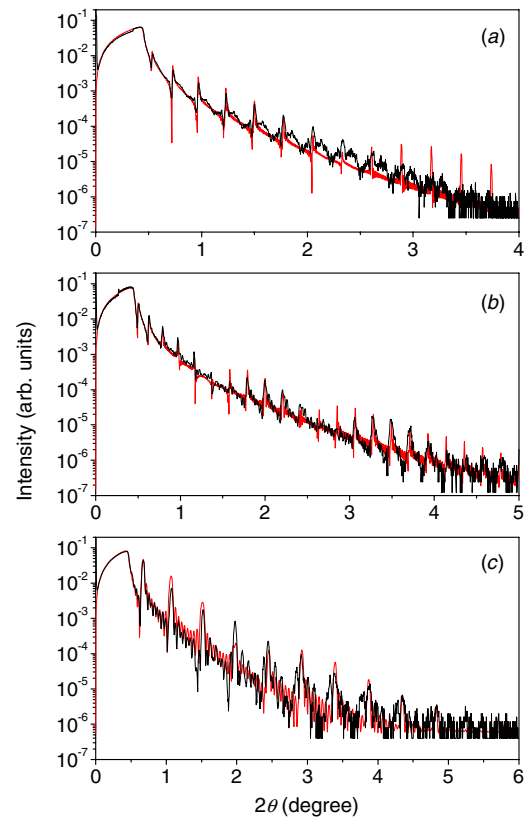


Figure 3. Experimental (black line) and simulated (red/grey line) (004) rocking curves from the $\text{Si}_{1-x}\text{Ge}_x/\text{Si}$ multilayers with (a) $x = 0.09$, (b) $x = 0.17$ and (c) $x = 0.53$. The simulated reflectivity curves were calculated using the structural parameters determined from the high resolution x-ray rocking curve analysis. Distinct roughness parameters σ_{Si} and σ_{Ge} , as given in table 1, were assigned to the Si to $\text{Si}_{1-x}\text{Ge}_x$ and $\text{Si}_{1-x}\text{Ge}_x$ to Si interfaces. These were assumed to be constant throughout the structures. The simulation also included a surface oxide layer of 0.6 nm roughness and 2 nm thickness for $x = 0.09$ and 0.17 and 1 nm thickness for $x = 0.53$.

curves of figure 2 correspond to the integrated intensity in a vertical direction, the RSM provides details on the actual shape of the various satellite features and reveals additional x-ray scattering away from Bragg conditions. In the RSM, the superperiodicity is revealed by the presence of equally spaced satellite spots aligned in a vertical direction. Interesting differences between samples can be noted by comparing the various RSMs of figure 4. First, the sample with $x = 0.091$ presents satellites that have the smallest full width $\Delta h = 0.0008$ in the h direction. Samples with $x = 0.17$ and 0.53 exhibit broader satellites with $\Delta h = 0.001$. More interestingly, the latter sample displays side lobes arising from a periodic modulation of the interfaces similar to that depicted in figure 1 and this is discussed in detail elsewhere [25, 26]. The sample with $x = 0.61$ exhibits broader diffuse satellites with $\Delta h = 0.002$. This RSM is typical of Ge-rich ($x > 0.6$) multilayers and indicates a significant loss of interfacial perfection and shorter coherence length, both parallel and perpendicular to the interface.

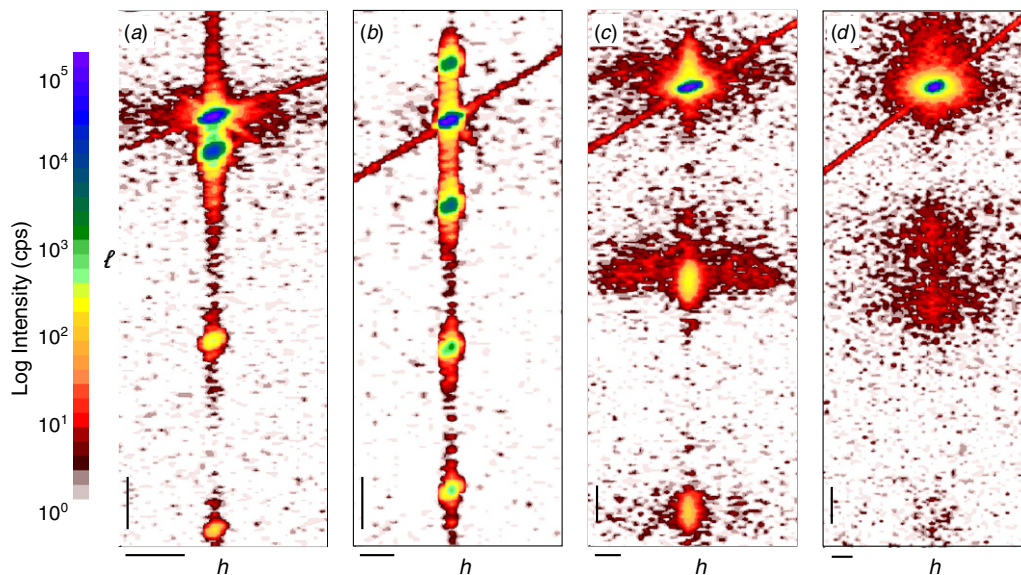


Figure 4. Reciprocal space maps about $(h, k, \ell) = (0, 0, 4)$ for four $\text{Si}_{1-x}\text{Ge}_x/\text{Si}$ multilayers with (a) $x = 0.09$, (b) $x = 0.17$ and (c) $x = 0.53$ and (d) $x \approx 0.6$. Here, the intensity is shown on a logarithmic scale. The horizontal and vertical scale markers correspond to $\Delta h = 0.001$ and $\Delta \ell = 0.005$, respectively.

3. Optical measurements

We have used an Ar^+ laser (458 nm) for steady-state PL excitation with the excitation intensity varied from 0.1 to 10 W cm^{-2} . The PL signal was dispersed using a single grating Acton Research 0.5 m monochromator and detected by a liquid nitrogen cooled InGaAs diode array in the spectral range 0.9–1.6 μm . The PL at longer wavelengths was measured using a single, liquid nitrogen cooled, InGaAs detector with a spectral sensitivity extending up to 2.6 μm . The measurements were performed in the temperature range 4–300 K. The time-resolved PL was excited using a pulsed laser diode with a wavelength of 680 nm and recorded using a Hamamatsu photomultiplier in the spectral range of 0.9–1.63 μm (0.76–1.38 eV). The signal was recorded using a LeCroy 915M digital oscilloscope with the background signal being independently measured and carefully subtracted. The excitation pulse duration was chosen to achieve nearly steady-state PL conditions. The overall time resolution of the entire system was better than 100 ns. Raman spectra were collected at room temperature in a back scattering geometry using an Ar^+ laser with 514, 505 and 458 nm lines as the excitation sources. The scattered light was analyzed using a Jobin-Yvon 1 m double monochromator equipped with a cooled photomultiplier and photon counting system.

4. Raman scattering and PL in $\text{Si}_{1-x}\text{Ge}_x$ nanostructures with $x < 0.60$

Figure 5 compares Raman spectra in samples with $\text{Si}_{1-x}\text{Ge}_x/\text{Si}$ 3D nanostructures with $0.09 < x < 0.55$. In $\text{Si}_{1-x}\text{Ge}_x$ islands with a low Ge content ($x = 0.091$), we observe a Raman signal attributed to Si–Si vibrations with a main, zone-center optical phonon peak at $\sim 520 \text{ cm}^{-1}$ and a weaker signal at $\sim 300 \text{ cm}^{-1}$

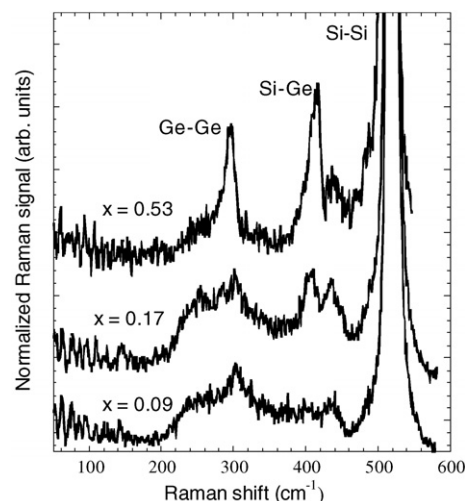


Figure 5. Evolution of Raman spectra in 3D $\text{Si}_{1-x}\text{Ge}_x/\text{Si}$ samples with x increasing from 0.09 to 0.53.

associated with Si acoustic phonons [28]. No significant Raman peaks associated with Ge–Ge vibrations at 290 cm^{-1} , Si–Ge vibrations at $\sim 420 \text{ cm}^{-1}$ [29] and to an amorphous Si phase at $\sim 480 \text{ cm}^{-1}$ [30] were found. An increase in the Ge content up to $x = 0.17$ increases the intensity of the Raman peak associated with Si–Ge vibrations at $\sim 420 \text{ cm}^{-1}$. However, the Raman signal associated with Ge–Ge vibrations at $\sim 310 \text{ cm}^{-1}$ is still quite weak. A further increase in the Ge content ($x = 0.53$) in 3D $\text{Si}_{1-x}\text{Ge}_x$ nanostructures produces strong Raman signals at $\sim 310 \text{ cm}^{-1}$ related to Ge–Ge vibrations, and at 420 cm^{-1} related to Si–Ge vibrations. Note that in the sample with $x = 0.53$, the Si–Si vibration-related peak at $\sim 520 \text{ cm}^{-1}$ broadens significantly, most likely due to an increase in built-in strain, which in $\text{Si}_{1-x}\text{Ge}_x/\text{Si}$ samples

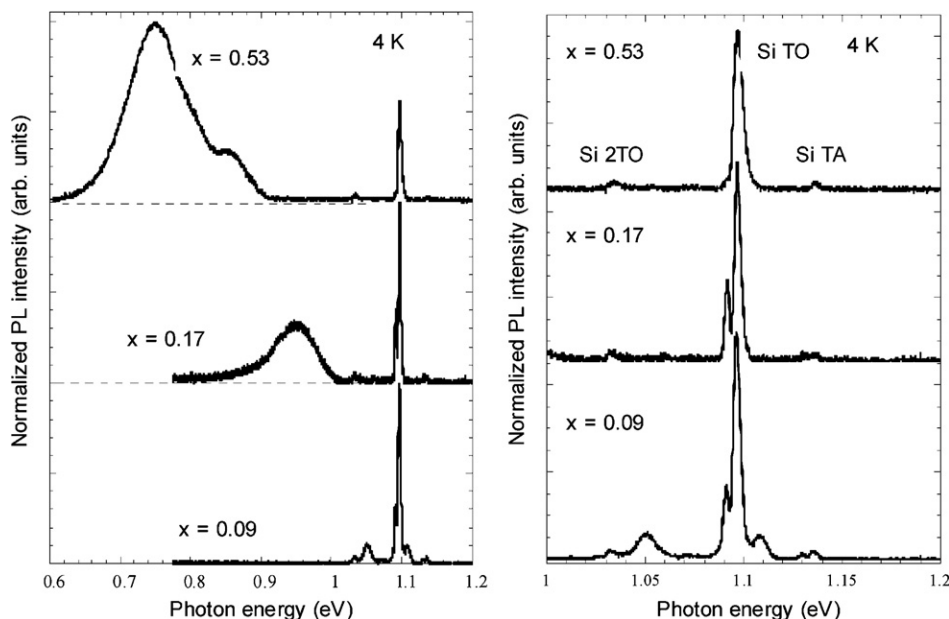


Figure 6. (Left) Low temperature (4 K) PL spectra in 3D $\text{Si}_{1-x}\text{Ge}_x/\text{Si}$ samples with x increasing from 0.09 to 0.53. (Right) High-resolution PL data showing changes in the Si-related PL as the Ge content increases.

with thicker Ge layers can be entirely localized within the Si spacer layers [31]. Another important observation is the absence of a-Si and a-Ge phases, showing that the islands in $\text{Si}_{1-x}\text{Ge}_x/\text{Si}$ multilayers are true crystalline alloys.

Figure 6 presents PL spectra in the same samples ($x = 0.091$, $x = 0.17$ and $x = 0.53$). In the sample with the lowest Ge content in $\text{Si}_{1-x}\text{Ge}_x/\text{Si}$ multilayers, the PL spectrum shows the signal related to c-Si transverse optical (TO) phonon replica near 1.1 eV and narrow PL bands at 1.05 and 1.11 eV attributed to no-phonon (NP) and TO phonon PL bands in Si-rich $\text{Si}_{1-x}\text{Ge}_x$ alloys [32, 33]. Note that these PL bands are in the vicinity of c-Si luminescence, and that the intensities of these two PL bands are comparable (figure 6 (left)). Most likely, a small amount of Ge (<10%) just slightly reduces the $\text{Si}_{1-x}\text{Ge}_x$ bandgap and relaxes the selection rules, and this increases the ratio of NP/TO PL band intensities. The observed broadening of these two PL bands is, apparently, due to the compositional disorder introduced by $\sim 10\%$ of Ge atoms in a crystalline Si matrix. Note that the main PL band associated with radiative carrier recombination in c-Si splits with a ~ 5 meV separation between the main PL peak and a weaker satellite peak (figure 6 (right)). A similar splitting has been reported in doped Si and associated with the formation of a bound exciton and/or a distortion of the Si lattice field [5].

An increase in the Ge content (from $x = 0.091$ to $x = 0.17$) changes the PL spectrum drastically. We find an intense PL band with the main peak at 0.95 eV, indicating a difference of ~ 150 meV between the bandgaps of pure c-Si and a crystalline $\text{Si}_{1-x}\text{Ge}_x$ alloy with $x = 0.17$. This broad and featureless PL band with a full width at half maximum (FWHM) of ~ 70 meV indicates a much stronger compositional disorder compared to the $\text{Si}_{1-x}\text{Ge}_x/\text{Si}$ sample with $x = 0.091$.

A further increase in the Ge content ($x = 0.53$) in 3D $\text{Si}_{1-x}\text{Ge}_x/\text{Si}$ nanostructures produces a broad, double-peak

PL spectrum with the major PL peak centered at a photon energy of 0.75 eV and the second PL peak at ~ 0.85 eV (figure 6 (left)). The low-temperature PL quantum efficiency in the samples with $x = 0.53$ is found to be the highest, of the order of 1% or better. Both PL bands are quite broad, most likely due to additional compositional disorder (and its variation) in Ge-rich $\text{Si}_{1-x}\text{Ge}_x$ islands: such a disorder can relax selection rules for optical transitions, decrease the radiative lifetime and, therefore, increase the PL quantum efficiency. The compositional disorder was originally postulated from a Raman and PL study of similar samples to comprise a non-uniform Ge distribution within the $\text{Si}_{1-x}\text{Ge}_x$ islands [34], and this proposition has since been confirmed by recent analytical TEM studies [24–26]. The PL peak associated with carrier recombination in Si spacer layers also broadens and slightly shifts to greater photon energy, indicating the presence of a strain field. Note that no PL peaks associated with structural defects (e.g., D-lines) [5] have been found in these measurements.

5. Raman scattering and PL for $\text{Si}_{1-x}\text{Ge}_x$ nanostructures with $x \geq 0.6$

We find drastic, step-like changes in the Raman spectra for $\text{Si}_{1-x}\text{Ge}_x/\text{Si}$ 3D nanostructures with x approaching or slightly greater than 0.6 (figure 7). First, the Raman signal strongly depends on the excitation wavelength (figure 7 (left)), and this most likely reflects structural changes in our samples as a function of the excitation penetration depth. Using 514 nm excitation, we observe all first-order Raman modes: Si–Si vibrations with a narrow peak at 520 cm^{-1} , most likely due to light scattering within the c-Si substrate; a sharp peak near 490 cm^{-1} associated with Si–Si vibrations with a neighboring Ge atom and two Raman peaks at ~ 400 and 300 cm^{-1}

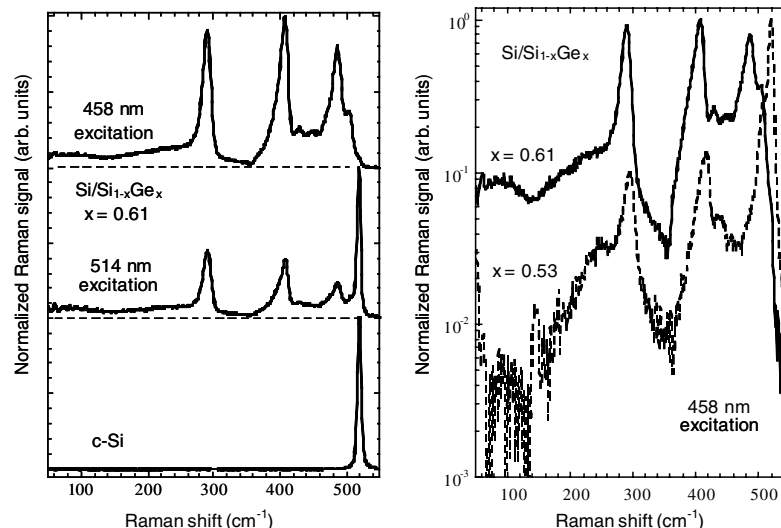


Figure 7. Raman spectra in 3D $\text{Si}_{1-x}\text{Ge}_x/\text{Si}$ samples with $x = 0.61$. (Left) Raman spectra collected at different excitation wavelengths and (right) a comparison between Raman data in samples with $x = 0.53$ and $x = 0.61$.

associated with Si–Ge and Ge–Ge vibrations, respectively. The highest intensity Raman peak associated with scattering within the $\text{Si}_{1-x}\text{Ge}_x/\text{Si}$ multilayers is at $\sim 300\text{ cm}^{-1}$.

When using 458 nm excitation, we find a nearly complete disappearance of the Raman peak at 520 cm^{-1} , a better pronounced fine structure of the Raman signal between 500 and 400 cm^{-1} , and an increase of the 490 cm^{-1} peak intensity. In addition, we observe a strong increase in the relative intensity of the Raman peak at $\sim 405\text{ cm}^{-1}$, which now becomes dominant (figure 7 (left)). Comparing Raman signals from the samples with $x = 0.53$ and $x = 0.61$ under 458 nm excitation (figure 7 (right)), we find a consistent shift of all major Raman peaks toward lower wave numbers as the Ge content increases.

Figure 8 compares steady-state PL spectra from 3D $\text{Si}_{1-x}\text{Ge}_x/\text{Si}$ multilayer samples with $x = 0.53$ and 0.61 . As the Ge content increases, we observe a strong PL blue shift and a decrease in the PL peak FWHM from ~ 100 to $\sim 50\text{ meV}$. In addition, the PL quantum efficiency decreases by at least an order of magnitude. Note that this behavior is inconsistent with the $0.09 < x < 0.55$ samples, where we observe a red PL shift, an increase of the FWHM and an increase of the PL quantum efficiency as x increases.

Figure 9 compares PL temperature dependences for samples with $x = 0.17$, 0.53 , 0.56 and 0.61 . For all these samples, the PL intensity is temperature independent at low temperature but at higher temperature it drops with thermal quenching activation energies estimated to be $\sim 25\text{ meV}$ for $x = 0.17$ and $\sim 60\text{ meV}$ for $x = 0.53$ and 0.56 . The sample with the lowest Ge content ($x = 0.091$) exhibits PL thermal quenching with an activation energy of $\sim 15\text{ meV}$ (see [34] for details). Qualitatively, the experimental data for the sample with $x = 0.61$ are quite similar to those in the sample with $x = 0.17$. Numerical fitting, however, indicates at least two PL thermal quenching activation energies in the temperature region from 30 to 200 K, estimated as being 20 meV and 60 meV, respectively. Naturally, a lower thermal quenching

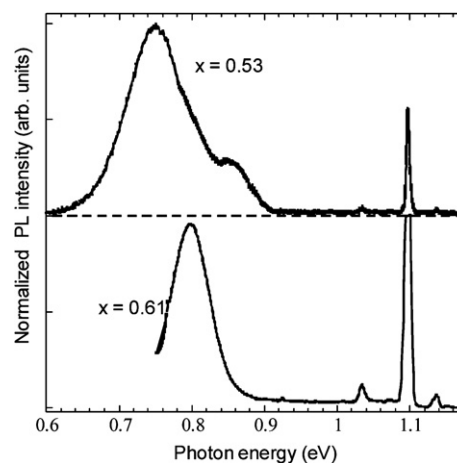


Figure 8. Low temperature (4 K) PL spectra in 3D $\text{Si}_{1-x}\text{Ge}_x/\text{Si}$ samples with $x = 0.53$ and $x = 0.61$.

activation energy results in a lower PL intensity at higher temperature; to emphasize this point, the temperature at which a 50% PL intensity reduction occurs is shown in figure 9(a) for the samples with composition $x = 0.17$, 0.53 and 0.56 .

6. Time-resolved PL

Figure 10 compares PL decays under pulsed excitation: we find a fast, microsecond-long PL in samples with $x = 0.17$ while samples with $x > 0.5$ show both short- and long-lived PL components with characteristic lifetimes in the range from $1\text{ }\mu\text{s}$ to 10 ms. A 10 ms PL lifetime is probably the longest ever reported in Si-based semiconductor nanostructures: it indicates an efficient carrier localization at the $\text{Si}/\text{Si}_{1-x}\text{Ge}_x$ interface, a limited overlap of electron–hole wavefunctions (most likely due to a type-II band alignment) and a nearly defect-free carrier recombination environment: details of the carrier recombination mechanism are discussed elsewhere

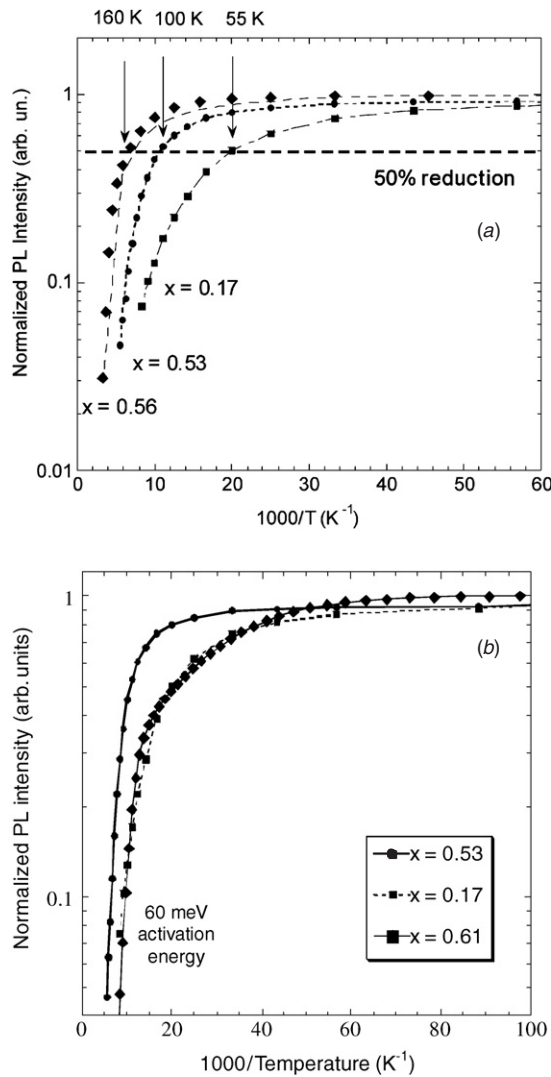


Figure 9. (a) PL temperature dependences in 3D Si_{1-x}Ge_x/Si samples with $x = 0.17$, 0.53 and 0.56 . Also indicated at the top are the temperatures at which the PL intensity has fallen to half maximum for these samples. (b) PL temperature dependences in 3D Si_{1-x}Ge_x/Si samples with $x = 0.17$, 0.53 and 0.61 . The region of the curves corresponding to an activation energy of 60 meV has been indicated.

[36]. Figure 11 summarizes the PL lifetime dependence on the detection photon energy, which is found only for the slow PL band: it decreases in magnitude by approximately ten times in the spectral range from 0.85 to 0.75 eV.

Time-resolved PL data in the sample with $x = 0.61$ is consistent with steady-state PL data: like the sample with $x = 0.17$, we find only a fast PL component with a microsecond lifetime.

7. PL intensity as a function of excitation intensity

Figure 12 shows the PL-integrated intensity recorded at 4 K as a function of the excitation intensity for Si_{1-x}Ge_x island samples with average Ge concentrations of $x = 0.17$ and

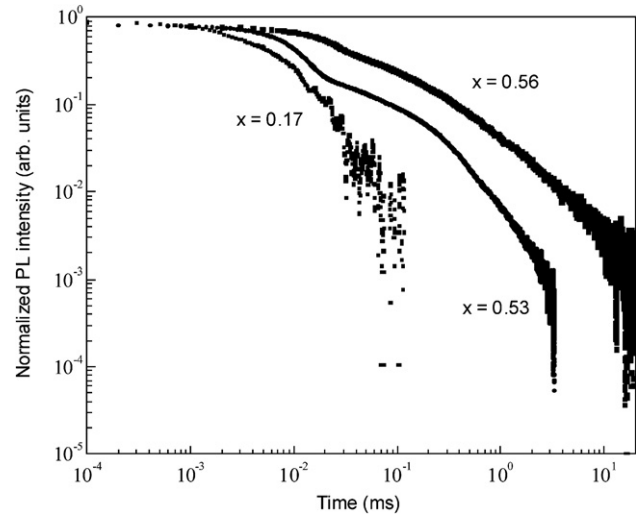


Figure 10. Low temperature (4 K) PL decays in 3D Si_{1-x}Ge_x/Si samples with $x = 0.17$, 0.53 and 0.55 [36]. Note the double logarithmic scale.

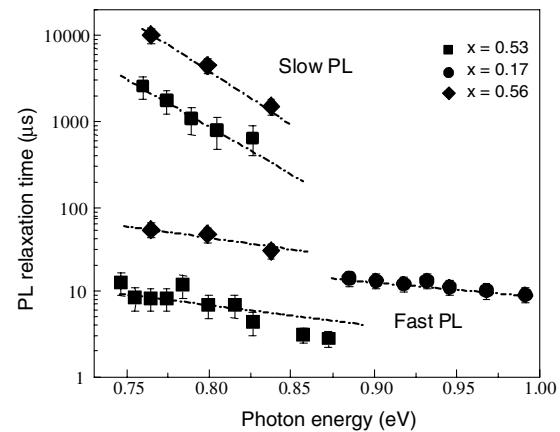


Figure 11. Summarized data on PL lifetime as a function of the detection photon energies in 3D Si_{1-x}Ge_x/Si samples with $x = 0.17$, 0.53 and 0.55 [36].

0.53 . The intensity of the Si PL band at ~ 1.1 eV in both samples is a linear function of the excitation intensity, while the PL intensity in Si_{1-x}Ge_x clusters shows a much weaker dependence. Since the entire region of the Si_{1-x}Ge_x cluster PL intensity covers less than one decade for the excitation intensities used in this study, it is not realistic to discuss a possible fit and specific function to approximate the experimental data. Most likely, however, the experimental results reflect a rapid PL intensity saturation due to a long carrier radiative lifetime and its competition with non-radiative Auger recombination. Interestingly, the PL intensity as a function of the excitation intensity saturates much faster in the sample with an average Ge concentration of $x = 0.17$ compared to that in the sample with $x = 0.53$. A complete physical model requires detailed measurements of the PL dynamics over a wide range of excitation intensities, and these will be presented elsewhere [35].

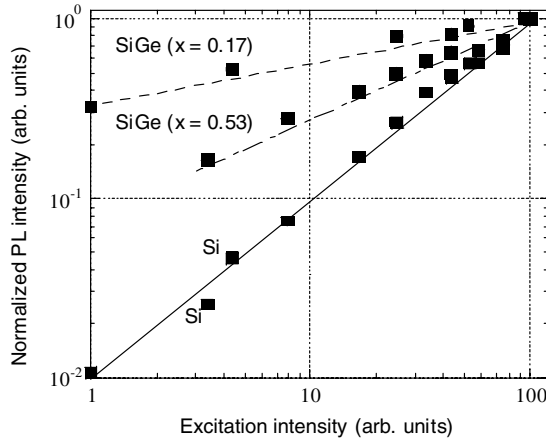


Figure 12. Normalized integrated PL intensity for the Si PL band (~ 1.1 eV) and $\text{Si}_{1-x}\text{Ge}_x$ PL bands (see figure 3(a)) as a function of the excitation intensity. The PL data have been recorded at 4 K for two $\text{Si}_{1-x}\text{Ge}_x$ island samples with average Ge compositions of $x = 0.17$ and $x = 0.53$, respectively. The Si band intensity exhibits a linear dependence on the excitation intensity, but the $\text{Si}_{1-x}\text{Ge}_x$ PL bands show a sublinear response.

8. Discussion

In the samples with $0.091 \leq x \leq 0.53$, we observe a consistent correlation between the Ge content in the $\text{Si}_{1-x}\text{Ge}_x$ 3D nanostructures and the PL properties: as the Ge content increases, the PL intensity temperature dependence exhibits a higher activation energy for thermal quenching as well as a higher PL quantum efficiency. We conclude that in the samples with a low Ge content (e.g., $x = 0.091$), the PL thermal quenching activation energy is comparable to the exciton binding energy (~ 10 meV), and carrier recombination is controlled by the thermal dissociation of an exciton localized at $\text{Si}_{1-x}\text{Ge}_x$ alloy structural fluctuations [33, 37]. The presence of these fluctuations is signified by the broadening of the x-ray diffraction peaks in the transverse direction due to a loss of translational symmetry in the plane of growth (see figure 4(a)). Such fluctuations have been seen before in similar low Ge content samples by Noël *et al* [38] and are postulated to exist in the form of Ge-rich ‘platelets’. These platelets with their incipient 3D characteristics are thus the precursors to the well-formed 3D islands that are observed at higher x values. In the samples with $x \geq 0.17$, carrier recombination mostly occurs at Si/Si $_{1-x}$ Ge $_x$ interfaces. A further increase in the Ge content leads to the formation of well-defined, quasi-type-II heterointerfaces with presumably a low energy barrier for electrons and a deep energy well for holes within the $\text{Si}_{1-x}\text{Ge}_x$ islands [39].

In the $x = 0.53$ sample, the PL spectrum contains two PL bands peaked at 0.85 eV and 0.75 eV respectively (see figure 8). There are no characteristic phonons in the $\text{Si}_{1-x}\text{Ge}_x/\text{Si}$ system with an energy of ~ 100 meV, and it is thus reasonable to assume that 3D $\text{Si}_{1-x}\text{Ge}_x/\text{Si}$ nanostructures with $x = 0.53$ contain coupled electron-hole subsystems. We assume that due to the type-II nature of the $\text{Si}_{1-x}\text{Ge}_x/\text{Si}$ heterointerface and a low energy barrier for electrons, the

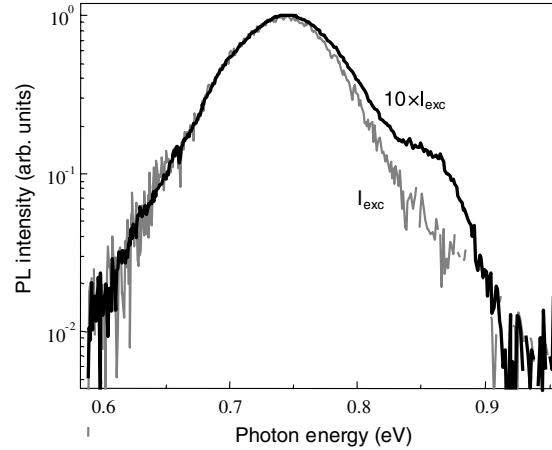


Figure 13. Low temperature (4 K) PL spectra in 3D $\text{Si}_{1-x}\text{Ge}_x/\text{Si}$ samples with $x = 0.53$ at different levels of photoexcitation. Note the logarithmic vertical scale.

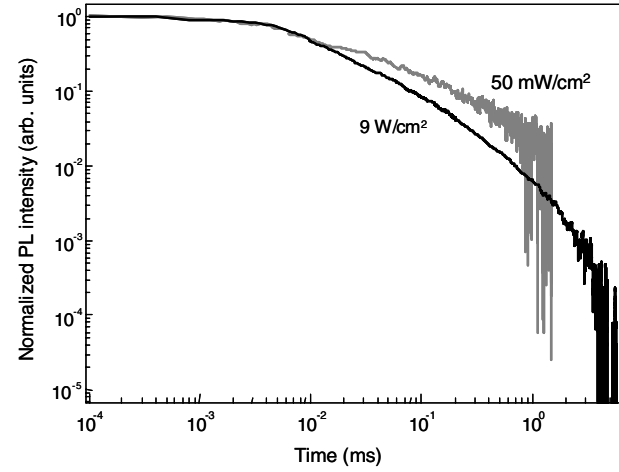


Figure 14. Low temperature (4 K) PL decays in 3D $\text{Si}_{1-x}\text{Ge}_x/\text{Si}$ samples with $x = 0.53$ at different levels of photoexcitation [36]. Note the double logarithmic scale.

latter, especially under high photoexcitation, can move over the barrier and directly recombine with holes localized within the $\text{Si}_{1-x}\text{Ge}_x$ islands. This assumption is supported by the coexistence of slow and fast PL decays and by the different intensity ratio between the PL bands at 0.75 and 0.85 eV at different levels of photoexcitation (see figure 13).

The observed coexistence of fast and slow PL components in Ge-rich ($x > 0.5$) samples is also explained by the $\text{Si}_{1-x}\text{Ge}_x/\text{Si}$ interface carrier recombination. According to our model [36], the fast PL component dominates in $\text{Si}_{1-x}\text{Ge}_x/\text{Si}$ heterostructures with type-II energy band alignment when a significant energy band bending is induced by the excess carriers produced under high photoexcitation. Under the same excitation conditions, the intensity of the PL band at 0.85 eV increases (see figure 13). However, by decreasing the excitation intensity we can markedly suppress the 0.85 eV PL band as well as the fast PL component (see figures 13 and 14). Therefore, we conclude that at high excess carrier concentration, most of the carriers recombine via a fast

recombination channel associated with dynamic (i.e. induced by carrier accumulation) type-I energy band alignment, while the type-II energy band alignment can only be confirmed by observing a slow PL decay at a low level of photoexcitation.

Increasing the Ge content up to $x = 0.61$ in $\text{Si}_{1-x}\text{Ge}_x$ alloy islands of only few monolayers in height, we observe a strong, step-like increase in strain (see the Raman spectra in figure 7). We think that such a high Ge content results in strain-induced Si/Ge interdiffusion, and that this affects the abruptness of the $\text{Si}_{1-x}\text{Ge}_x/\text{Si}$ interfaces. The x-ray measurements for this sample indicate that there is, indeed, a pronounced smearing of the $\text{Si}_{1-x}\text{Ge}_x/\text{Si}$ interfaces (see section 2). Therefore, these samples exhibit PL properties more similar to $\text{Si}_{1-x}\text{Ge}_x$ alloys with a structureless PL band and having only a fast PL component [35].

It has been noted that a PL temperature dependence with a thermal quenching activation energy close to 15 meV has been associated in Si-rich $\text{Si}_{1-x}\text{Ge}_x$ alloys with thermal dissociation of an exciton localized on compositional fluctuations, while a greater activation energy in Ge richer samples has been connected with the valence band energy barriers at the $\text{Si}/\text{Si}_{1-x}\text{Ge}_x$ interface [33, 37]. Here, we note that the observed activation energies do not match the estimated $\text{Si}/\text{Si}_{1-x}\text{Ge}_x$ energy band barriers: the conduction band energy barrier at the $\text{Si}/\text{Si}_{1-x}\text{Ge}_x$ heterointerface is estimated to be < 10 meV [36], and PL spectra indicate the discontinuity of the valence band to be $E_{\text{BG}}^{\text{Si}} - E_{\text{PL}} \approx 0.3$ eV. We suggest that in Ge-rich $\text{Si}/\text{Si}_{1-x}\text{Ge}_x$ samples, carrier diffusion as well as non-radiative carrier recombination are limited by both hole thermionic emission and hole tunneling (most likely phonon-assisted tunneling) through the valence band energy barriers. It is also possible that, in the samples with $x > 0.6$, the strain and strain-induced interdiffusion modifies the $\text{Si}/\text{Si}_{1-x}\text{Ge}_x$ interface locally; thus, such samples exhibit significant spatial variations in their PL properties. To complete the formulation of an appropriate physical model, detailed measurements of the PL dynamics over a wide range of excitation intensities and the mapping of PL properties with a submicron spatial resolution are needed, and these will be presented elsewhere [35].

9. Conclusion

We present Raman and PL studies in 3D multilayer $\text{Si}_{1-x}\text{Ge}_x/\text{Si}$ samples with precise control over the $\text{Si}_{1-x}\text{Ge}_x$ chemical composition in the range $0.091 \leq x \leq 0.61$. We find that Si-rich alloy nano-islands ($x < 0.1$) exhibit optical properties similar to Si-rich $\text{Si}_{1-x}\text{Ge}_x$ bulk alloys. According to our data, better defined $\text{Si}_{1-x}\text{Ge}_x/\text{Si}$ interfaces are formed when x approaches 0.50. Also, our PL data strongly indicate that in samples with $x \approx 0.5$, radiative carrier recombination takes place at these heterointerfaces. Apparently, a limited overlap of electron-hole wavefunctions for carriers localized at the type-II $\text{Si}_{1-x}\text{Ge}_x/\text{Si}$ heterointerface is responsible for an unusually long-lived PL component (up to 10 ms). A faster, microsecond, PL is found to coexist with the long-lived PL: it is attributed to electron transitions to $\text{Si}_{1-x}\text{Ge}_x$ islands at a high level of photoexcitation and quasi-direct recombination

with holes localized within $\text{Si}_{1-x}\text{Ge}_x$ islands. A higher than 60% Ge content increases the strain and strain-induced Si/Ge interdiffusion; therefore, the $\text{Si}_{1-x}\text{Ge}_x/\text{Si}$ interface profile is, probably, affected. As a result, the PL in these samples is similar to the PL in Ge-rich bulk $\text{Si}_{1-x}\text{Ge}_x$ alloys.

Acknowledgments

The work at NJIT is supported by the National Science Foundation, Intel Corporation and the Foundation at NJIT. Two of the samples discussed here were grown by Dr J P Noël and we acknowledge this contribution. We also thank Dr X Wu for providing the TEM micrograph of a $\text{Si}_{1-x}\text{Ge}_x/\text{Si}$ island superlattice.

References

- [1] Lockwood D J 1998 *Light Emission in Silicon: From Physics to Devices* (San Diego: Academic)
- [2] Canham L T 1990 *Appl. Phys. Lett.* **57** 1046
- [3] Ennen H, Schneider J, Pomrenke G and Axmann A 1983 *Appl. Phys. Lett.* **43** 943
- [4] Kamenev B V, Timoshenko V Yu, Konstantinova E A, Kudoyarova V Kh, Terukov E I and Kashkarov P K 2002 *J. Non-Cryst. Solids* **299–302** 668
- [5] Davies G 1989 *Phys. Rep.* **176** 83
- [6] Bradfield P L, Brown T G and Hall D G 1988 *Phys. Rev. B* **38** 3533
- [7] Zachai R, Eberl K, Abstreiter G, Kasper E and Kibbel H 1990 *Phys. Rev. Lett.* **64** 1055
- [8] Sturm J C, Manoharan H, Lenchyshyn L C, Thewalt M L W, Rowell N L, Noël J-P and Houghton D C 1991 *Phys. Rev. Lett.* **66** 1362
- [9] Apetz R, Vescan L, Hartmann A, Dieker C and Lüth H 1995 *Appl. Phys. Lett.* **66** 445
- [10] Teichert C, Lagally M G, Peticolas L J, Bean J C and Tersoff J 1996 *Phys. Rev. B* **53** 16334
- [11] Floro J A, Chason E, Twisten R D, Hwang R Q and Freund L B 1997 *Phys. Rev. Lett.* **79** 3946
- [12] Sutter P and Lagally M G 1998 *Phys. Rev. Lett.* **81** 3471
- [13] Tromp R M, Ross F M and Reuter M C 2000 *Phys. Rev. Lett.* **84** 4641
- [14] Schmidt O G and Eberl K 2000 *Phys. Rev. B* **61** 13721
- [15] Stangl J, Holý V, Roch T, Daniel A, Bauer G, Zhu J, Brunner K and Abstreiter G 2000 *Phys. Rev. B* **62** 7229
- [16] Capellini G, De Seta M and Evangelisti F 2001 *Appl. Phys. Lett.* **78** 303
- [17] Apetz R, Vescan L, Hartmann A, Dieker C and Lüth H 1995 *Appl. Phys. Lett.* **66** 445
- [18] Brunner J, Rupp T S, Gossner H, Ritter R, Eisele I and Abstreiter G 1994 *Appl. Phys. Lett.* **64** 994
- [19] Baribeau J-M, Jackman T E, Houghton D C, Maigné P and Denhoff M W 1988 *J. Appl. Phys.* **63** 5738
- [20] Baribeau J-M, Lockwood D J, Dharma-wardana M W C, Rowell N L and McCaffrey J P 1989 *Thin Solid Films* **183** 17
- [21] Shin H K, Lockwood D J and Baribeau J-M 2000 *Solid State Commun.* **114** 505
- [22] Lockwood D J, Wu X and Baribeau J-M 2007 *IEEE Trans. Nanotech.* **6** 245
- [23] Parrat L G 1954 *Phys. Rev.* **95** 359
- [24] Baribeau J-M, Wu X, Rowell N L and Lockwood D J 2006 *J. Phys.: Condens. Matter* **18** R139
- [25] Baribeau J-M, Wu X and Lockwood D J 2006 *J. Vac. Sci. Technol. A* **24** 663

- [26] Baribeau J-M, Wu X and Lockwood D J 2007 *Mater. Res. Soc. Proc.* **958** 119
- [27] Croce P and Nevot L 1976 *Rev. Phys. Appl.* **11** 113
- [28] Temple P A and Hathaway C E 1973 *Phys. Rev. B* **7** 3685
- [29] Alonso M I and Winer K 1989 *Phys. Rev. B* **39** 10056
- [30] Smith J E Jr, Brodsky M H, Crowder B L, Nathan M I and Pinczuk A 1971 *Phys. Rev. Lett.* **26** 642
- [31] Kamenev B V, Grebel H, Tsybeskov L, Kamins T I, Stanley Williams R, Baribeau J-M and Lockwood D J 2003 *Appl. Phys. Lett.* **83** 5035
- [32] Zrenner A, Frohlich B, Brunner J and Abstreiter G 1995 *Phys. Rev. B* **52** 16608
- [33] Tilly L P, Mooney P M, Chu J O and LeGoues F K 1995 *Appl. Phys. Lett.* **67** 2488
- [34] Kamenev B V, Tsybeskov L, Baribeau J-M and Lockwood D J 2004 *Appl. Phys. Lett.* **84** 1293
- [35] Kamenev B V *et al* 2008 unpublished
- [36] Kamenev B V, Tsybeskov L, Baribeau J-M and Lockwood D J 2005 *Phys. Rev. B* **72** 193306
- [37] Sunamura H, Shiraki Y and Fukatsu S 1995 *Appl. Phys. Lett.* **66** 953
- [38] Noël J P, Rowell N L, Houghton D C, Wang A and Perovic D D 1992 *Appl. Phys. Lett.* **61** 690
- [39] Paul D J 1999 *Adv. Mater.* **11** 191